




Compressive frequency-difference direction-of-arrival estimation

Jeung-Hoon Lee,¹  Yongsung Park,^{2,a)}  and Peter Gerstoft² 

¹*School of Mechanical Engineering, Changwon National University, Uichang-gu, Changwon 51140, South Korea*

²*Scripps Institution of Oceanography, University of California at San Diego, La Jolla, California 92093-0238, USA*

ABSTRACT:

Direction-of-arrival estimation is difficult for signals spatially undersampled by more than half the wavelength. Frequency-difference beamforming [Abadi, Song, and Dowling (2012). *J. Acoust. Soc. Am.* **132**, 3018–3029] offers an alternative approach to avoid such spatial aliasing by using multifrequency signals and processing them at a lower frequency, the difference-frequency. As with the conventional beamforming method, lowering the processing frequency sacrifices spatial resolution due to a beam broadening. Thus, unconventional beamforming is detrimental to the ability to distinguish between closely spaced targets. To overcome spatial resolution deterioration, we propose a simple yet effective method by formulating the frequency-difference beamforming as a sparse signal reconstruction problem. Similar to compressive beamforming, the improvement (compressive frequency-difference beamforming) promotes sparse nonzero elements to obtain a sharp estimate of the spatial direction-of-arrival spectrum. Analysis of the resolution limit demonstrates that the proposed method outperforms the conventional frequency-difference beamforming in terms of separation if the signal-to-noise ratio exceeds 4 dB. Ocean data from the FAF06 experiment support the validity. © 2023 Acoustical Society of America. <https://doi.org/10.1121/10.0020053>

(Received 19 January 2023; revised 7 June 2023; accepted 16 June 2023; published online 11 July 2023)

[Editor: Paul J. Gendron]

Pages: 141–151

I. INTRODUCTION

Direction-of-arrival (DOA) estimation refers to the process of finding the direction of acoustic/electromagnetic sources from the outputs of a receiving sensor array and is an active field of research in signal processing and acoustics (Gerstoft *et al.*, 2018). Conventional beamforming (CBF) is the simplest and most popular DOA estimation method despite its low spatial resolution and sidelobe contamination. There are many methods designed to overcome the limitations of CBF, such as minimum variance distortionless response (MVDR) (Capon, 1969) and multiple signal classification (MUSIC) (Schmidt, 1986) among others. However, these adaptive methods are only applicable in several demanding scenarios, including low background noise, incoherent sources, and many snapshots. For a thorough review, readers are encouraged to refer to Krim and Viberg (1996) and Van-Trees (2002). All these beamformers are processed within the bandwidth of the measured signal. When a sensor array spatially undersamples signals by more than half the wavelength of the wave, aliased DOAs other than the true DOAs can appear. This spatial aliasing limits conventional beamformers at higher frequency. In addition, high-frequency processing is prone to performance degradation due to the mismatch between the actual and presumed signal wavefronts.

Recently, frequency-difference beamforming (FD) was introduced by Abadi *et al.* (2012). FD assumes

multifrequency data. Specifically, it obtains FD using the Hadamard product, which is an element-wise vector product between array data at lower frequency and complex-conjugated array data at higher frequency. The Hadamard product mimics a lower out-of-band acoustic wave field at the difference-frequency, which is the difference between the two frequencies used to form it (Worthmann *et al.*, 2015). Lowering the processing frequency gives robustness against spatial aliasing and wavefront mismatch, thereby, opening new opportunities when in-band beamforming is not suitable. The performance of FD is comparable to that of the conventional in-band beamformer (Abadi *et al.*, 2012; Douglass *et al.*, 2017; Douglass and Dowling, 2019; Xie *et al.*, 2020; Kim *et al.*, 2023). The extension of the frequency-difference idea to matched field processing has resulted in successful source localization in both shallow (Worthmann *et al.*, 2015) and deep (Geroski and Dowling, 2019; Geroski *et al.*, 2021; Worthmann and Dowling, 2017) oceans. For the DOA estimation, Kim *et al.* (2023) proposes a frequency-difference versus wavenumber analysis by adopting the frequency-difference concept.

For decreasing difference-frequency, the beam becomes wider, making it difficult for FD to resolve closely spaced DOAs. To improve the FD resolution, Xie *et al.* (2020) proposes post-processing the beamformed output of FD using the deconvolution technique described in Yang (2018). The source distribution is recovered through iterative deconvolution, where the shift-invariant FD beam pattern is treated as a point-spreading function. However, the deconvolution method assumes the existence of incoherent sources and

^{a)}Electronic mail: yongsungpark@ucsd.edu

only works for a uniformly spaced array. For more general non-uniform cases, the invariant point-spreading function should be replaced with a position-dependent function, thus, complicating the relevant algorithm.

A subspace-based (MUSIC) beamformer was implemented in our recent work to improve resolution (Park *et al.*, 2022). In the present study, a different approach is taken by employing sparse processing known as compressive sensing (CS). It has been successfully applied to determine the DOA of incoming signals by solving the least squares problem with l_1 -norm sparse-promoting constraint, that is, the least absolute shrinkage and selection operator (LASSO) problem (Gerstoft *et al.*, 2015; Malioutov *et al.*, 2005; Xenaki *et al.*, 2014). CS works well for challenging scenarios with coherent sources and a few snapshots (or even a single snapshot). Most importantly, the sparsity constraint obtains a sharp estimate of the beamforming spectrum that exhibits super-resolution of the DOA solution.

Our formulation, designated as compressive frequency-difference beamforming (CFD), replaces the field measurement vector in CS with the Hadamard product vector and evaluates the sensing matrix formed by steering vectors for all potential look angles at the difference-frequency. If CS is the counterpart of CBF, then CFD can be regarded as that of FD. Because CFD inherits the benefits of CS intact, no restrictions are imposed on the source characteristics or sensor spacing. Therefore, this study establishes one possible method for improving the resolution of FD.

The remainder of this paper is organized as follows. In Sec. II, we develop the details of CFD with a brief description of FD. Performance verifications through simulations and real ocean experiments are discussed in Sec. III.

II. METHOD

We consider K acoustic plane waves impinging upon a uniform linear array (ULA) comprising M sensors with spacing d . The k th source characterized by DOA $\theta_k \in [-90^\circ, 90^\circ]$ (0° is broadside) along with the complex strength x_k is assumed to possess a broad bandwidth from f_L to f_U with f being the source frequency in hertz. The phase delay from the k th source to each of the M sensors of the array is described by the following steering vector:

$$\mathbf{a}(\theta_k, f) = \frac{1}{\sqrt{M}} \begin{bmatrix} 1 & e^{-j(2\pi f/c)d \sin \theta_k} & e^{-j(2\pi f/c)2d \sin \theta_k} \\ \dots & e^{-j(2\pi f/c)(M-1)d \sin \theta_k} \end{bmatrix}^T \in \mathbb{C}^M, \quad (1)$$

where c is the sound speed, superscript T is the transpose, and $j = \sqrt{-1}$. Normalization with \sqrt{M} is introduced to simplify the analysis. The frequency domain representation of the array data $\mathbf{y} \in \mathbb{C}^M$ is

$$\mathbf{y} = \sum_{k=1}^K \mathbf{a}(\theta_k, f) x_k + \mathbf{n}, \quad (2)$$

where $\mathbf{n} \in \mathbb{C}^M$ is the additive Gaussian noise, which is assumed independent across the sensors.

A. FD

In the FD method, the frequency-difference Hadamard product, $\mathbf{z} \in \mathbb{C}^M$, is defined as the element-wise multiplication of frequency domain complex amplitudes at frequencies f_l and the complex conjugation of f_u ($f_l < f_u$). The product is expressed as

$$\mathbf{z} = \mathbf{y}(f_u) \circ \mathbf{y}^*(f_l), \quad (3)$$

where the symbol “ \circ ” denotes the element-wise (Hadamard) vector product, and “ $*$ ” denotes complex conjugation. The term “frequency-difference Hadamard product” is abbreviated as “Hadamard product” because the frequency-sum Hadamard product (Worthmann and Dowling, 2017) is not considered in this study. Note that the two frequencies f_u and f_l in constructing the product should be within the signal bandwidth $f_L \leq f_l, f_u \leq f_U$. The frequency range for the center frequency $f_c = (f_u + f_l)/2$ and difference-frequency $\Delta f = f_u - f_l$ is given by $f_L + \Delta f/2 \leq f_c \leq f_U - \Delta f/2$ and $0 \leq \Delta f \leq f_U - f_L$.

The Hadamard product mimics the solution of the Helmholtz equation at the difference-frequency (Worthmann and Dowling, 2017). The proof is easy for a plane wave given by $y(f, \mathbf{r}) = x(f) \exp(j2\pi f \mathbf{e}_s \cdot \mathbf{r})$, where $x(f)$ is the complex source amplitude that may depend on the frequency, \mathbf{e}_s is the unit vector along the direction of propagation, and \mathbf{r} is the location of the field point. Then the Hadamard product field is given by $y(f_u, \mathbf{r}) y^*(f_l, \mathbf{r}) = x(f_u) x^*(f_l) \exp(j2\pi \Delta f \mathbf{e}_s \cdot \mathbf{r})$. Although the unit and amplitude differ from the true out-of-band field that the product aims to emulate, this still describes a plane wave at Δf .

CBF quantifies the similarity between the steering vector $\mathbf{a}(\theta, f)$ and the measured pressure vector \mathbf{y} by changing the look angle θ . Thus, a natural choice for forming the FD beampower (B_{FD}) is to use \mathbf{z} instead of \mathbf{y} and compute the steering vector \mathbf{a} at Δf . In other words,

$$B_{FD}(\theta) = |\mathbf{a}^H(\theta, \Delta f) \mathbf{z}|^2, \quad (4)$$

where superscript H denotes the Hermitian transpose. B_{FD} is maximized when the look angle of the steering vector coincides with the direction of the plane wave source or with the true DOA. Since Δf is much lower than the in-band signal frequencies, it is typically chosen such that the corresponding wavelength $\Delta \lambda (= c/\Delta f)$ satisfies the aliasing free condition $d < \Delta \lambda/2$. Beam formation at a low downshifted frequency allows FD to be applied to a sparse array that is inaccessible with CBF and secures more robustness against potential errors in wave-field modeling.

One feature of the Hadamard product [Eq. (3)] is the occurrence of unintended cross-terms that lead to ghost DOAs in addition to the true ones. These ghost DOAs, denoted by θ_g , are distinct from the aliased DOAs that arise from violating the spatial Nyquist criterion. Among the K^2 terms produced by the quadratic product with K sources, K self-terms correspond to the true DOAs, and the remaining $K(K-1)$ cross-terms correspond to unintended ghost DOAs

that depend explicitly on the frequency. θ_g can be determined by solving Eq. (5) in Park *et al.* (2022), resulting in

$$\sin \theta_g = \frac{(2\pi f_u \sin \theta_i - 2\pi f_l \sin \theta_j)d/c}{2\pi \Delta f d/c}$$

$$i, j = 1, 2, \dots, K \ (i \neq j).$$

A term $2\pi l$ ($l=0, \pm 1, \pm 2, \dots$) is added on the right side to obtain the principal value of θ_g , ensuring that the argument of arcsine exists within ± 1 ($\pm 90^\circ$) (Yang *et al.*, 2021). Thus,

$$\theta_g = \sin^{-1} \left(\frac{(f_u \sin \theta_i - f_l \sin \theta_j)d/c + l}{\Delta f d/c} \right)$$

$$i, j = 1, 2, \dots, K \ (i \neq j), \quad (5)$$

where only a single valid integer l satisfies $|((f_u \sin \theta_i - f_l \sin \theta_j)d/c + l)/(\Delta f d/c)| < 1$.

Recent investigations have focused on ghost DOAs (Geroski and Worthmann, 2021; Wang *et al.*, 2022; Yang *et al.*, 2021). However, a simple method to mitigate these artifacts is to incoherently average Eq. (4) over the frequencies in the signal bandwidth. If variations for each of the two frequencies (f_l and f_u , or f_c and Δf) are possible, the broadband version of Eq. (4) can be written as

$$\bar{B}_{FD}(\theta) = \langle |\mathbf{a}^H(\theta, \Delta f) \mathbf{z}|^2 \rangle_{f_c, \Delta f}, \quad (6)$$

where $\langle \rangle_{f_c, \Delta f}$ denotes the double average over the range of f_c and Δf . The averaging process only suppresses unwanted interference without affecting the desired true DOA due to its frequency independence. The FD formulation described here is based on single-snapshot ($L=1$) data. The suppression of ghost DOAs is achievable even with a single-snapshot if the signal bandwidth is wide enough. For cases where multiple snapshots ($L>1$) are available, the single-snapshot \bar{B}_{FD} can be further averaged through snapshots, which enhances the stability of the beamforming output.

Although FD attains robustness with a difference-frequency Δf that is lower than the signal bandwidth, it sacrifices spatial resolution due to a wider beam width. It is not easy for FD to achieve the desired angular resolution, particularly when two or more DOAs are present in the same beam. Section II B discusses how we can improve the resolution capability of FD without sacrificing its robustness.

B. CFD

CS is a technique derived from information theory that can solve underdetermined inverse problems by assuming that the solution is sufficiently sparse. Sparse signal processing is applicable to the acoustic beamforming problem as sources occupy a small extent within a space. By exploiting this property, CS has been successfully applied to DOA estimation as compressive beamforming (Xenaki *et al.*, 2014). It solves a minimization problem with l_1 -norm sparsity-promoting regularizer, also known as the LASSO

(Tibshirani, 1996; Xenaki *et al.*, 2014). By using the model [Eq. (2)], the solution \mathbf{x} to observed data \mathbf{y} at frequency f can be written as

$$\mathbf{x}_{CS} = \arg \min_{\mathbf{x} \in \mathbb{C}^N} \|\mathbf{y} - \mathbf{A}(f)\mathbf{x}\|_2^2 + \mu \|\mathbf{x}\|_1. \quad (7)$$

Here, $\|\mathbf{x}\|_p = (\sum_{n=1}^N |x_n|^p)^{1/p}$ denotes the l_p -norm. Regularization parameter μ (>0) balances relative contribution between the fidelity (goodness of fit to the measurement) and the sparsity of the unknown vector $\mathbf{x} = [x_1(f), x_2(f), \dots, x_N(f)]^T \in \mathbb{C}^N$ comprising the complex source strengths for all N look angles $[\theta_1, \dots, \theta_N]$ at frequency f . The sensing matrix $\mathbf{A}(f) = [\mathbf{a}(\theta_1, f), \mathbf{a}(\theta_2, f), \dots, \mathbf{a}(\theta_N, f)] \in \mathbb{C}^{M \times N}$ is composed by collecting steering vectors for the same look angles and same frequency f . The DOA spectrum drawn by \mathbf{x}_{CS} indicates a super-resolution characteristic owing to l_1 -norm regularization.

To improve the spatial resolution of FD, we propose CFD by replacing \mathbf{y} with \mathbf{z} ,

$$\mathbf{x}_{CFD} = \arg \min_{\mathbf{x} \in \mathbb{C}^N} \|\mathbf{z} - \mathbf{A}(\Delta f)\mathbf{x}\|_2^2 + \mu \|\mathbf{x}\|_1, \quad (8)$$

where the sensing matrix \mathbf{A} is evaluated at the difference-frequency, $\mathbf{A}(\Delta f) = [\mathbf{a}(\theta_1, \Delta f), \mathbf{a}(\theta_2, \Delta f), \dots, \mathbf{a}(\theta_N, \Delta f)]$. Although the unknown solution vector in both Eqs. (7) and (8) is expressed as \mathbf{x} for a neat expression, the quadratic quantity \mathbf{x}_{CFD} is in a different unit than \mathbf{x}_{CS} . CFD is a sparse representation of FD; likewise, CS is a sparse representation of CBF.

No significant modifications have been made to the LASSO objective function, except for the observation vector and evaluation frequency. This enables CFD to preserve the advantages of CS, offering not only superior spatial resolution but also applicability for coherent arrivals or/and single snapshot. However, the limitations of CS related to basis mismatch and basis coherence also apply to CFD, as discussed in Xenaki *et al.* (2014).

The problem [Eq. (8)] is solved by a convex optimization routine implemented in open-source software, such as CVX (Grant and Boyd, 2014) and l_1 -MAGIC (Candes and Romberg, 2005). If successful, \mathbf{x}_{CFD} appears with K^2 -sparse signal ($K^2 \ll N$), that is, its components are zero or close to zero except few K^2 nonzero entries. Note that the solution of the LASSO problem undergoes attenuation in amplitude due to the regularization term (Gerstoft *et al.*, 2015; Wright, 2009; Xenaki *et al.*, 2014). As a post-processing step, it is necessary to debias the amplitude estimates by solving the following overdetermined problem:

$$\hat{\mathbf{x}}_{CFD} = \mathbf{A}_M^+(\Delta f) \mathbf{z}, \quad (9)$$

where $\mathbf{A}_M \in \mathbb{C}^{M \times K^2}$ is a tall matrix with collected K^2 columns of \mathbf{A} with indices of nonzero entries of \mathbf{x}_{CFD} , and “+” denotes the pseudo (left) matrix inverse. The squared amplitude of $\hat{\mathbf{x}}_{CFD}$ is designated as the beamforming output of CFD, $B_{CFD}(\theta) = |\hat{\mathbf{x}}_{CFD}|^2$, which is comparable to B_{FD} in Eq. (4).

As B_{CFD} is estimated per frequency sequentially, incoherent averages over the frequencies in the signal bandwidth are performed to mitigate unwanted interferences, including the ghost DOAs. The counterpart of \bar{B}_{FD} in Eq. (6) is given by

$$\bar{B}_{CFD}(\theta) = \langle |\hat{\mathbf{x}}_{CFD}|^2 \rangle_{f_c, \Delta f}. \quad (10)$$

Similar to the FD formulation, Eq. (10) refers to a single-snapshot case. For multiple snapshots, additional incoherent averages can be performed across the snapshots.

III. VALIDATION

A. Simulation

Performance verification of CFD is carried out with the setup shown in Fig. 1, where a ULA with $M=16$ sensors and spacing $d=3.75$ m is in a free-space water environment. The maximum allowable frequency to avoid ambiguities, that is, the spatial Nyquist frequency, is 0.2 kHz with sound speed $c=1500$ m/s. We consider two-plane wave sources, S1 and S2, with equal strengths and coming from directions θ_1 and θ_2 . θ_1 is fixed at 0° , while θ_2 parametrically varies between 0° and 25° to evaluate the separation capability of the proposed scheme. The frequency bandwidth of the sources is between 10 kHz ($=f_L$) and 20 kHz ($=f_U$). In this range, the considered array becomes sparse ($d/\lambda=25\text{--}50$), which makes conventional methods (CBF, CS) unsuitable. Twenty snapshots ($L=20$) of \mathbf{y} are generated by using the signal model [Eq. (2)]. The signal-to-noise ratio (SNR) $=20\log_{10}(E[\|\sum_{k=1}^K \mathbf{a}(\theta_k)x_k\|_2^2]/E[\|\mathbf{n}\|_2^2])$ is assumed as 30 dB.

The angular search interval is $\theta \in [-90^\circ, 90^\circ]$ with grid spacing of 0.1° , $N=1801$. For frequency averaging, we use a constant difference-frequency by setting Δf to the spatial Nyquist frequency of 0.2 kHz. The following overlapping rule is applied to increase the number of

averages, to suppress the effect of cross-terms as much as possible:

$$\begin{aligned} f_l &= (1-q)(i-1)\Delta f + f_L \\ f_u &= [(1-q)(i-1) + 1]\Delta f + f_L \end{aligned} \quad (i=1, 2, \dots, F), \quad (11)$$

where $q < 1$ is the overlap ratio, and $F = 1 + (f_U - f_L - \Delta f) / [(1-q)\Delta f]$ is the number of difference-frequency pairs. The ratio is set as $q=75\%$ ($F=197$), and no significant change was observed in the simulation results above this value.

CVX toolbox (Grant and Boyd, 2014) is employed to solve the CFD problem in Eq. (8). After conducting several trials, the proper value of the regularization parameter is determined as $\mu=0.1$, using the L-curve method (Kim and Nelson, 2004). While fine-tuning for each difference-frequency pair is recommended, the predetermined value is kept constant throughout the simulation. Varying by several tens of percent from the preset does not cause notable change in the results below.

In the first simulation, the two sources are incoherent, and their relative phase is uniformly distributed between 0 and 2π ($U[0, 2\pi]$). Figure 2 shows a comparison of FD and CFD for representative cases. The left panel represents the snapshot-averaged beampower B in the two-dimensional (2D) map versus look angle θ and center frequency of difference-frequency f_c . The FD maps mainly consist of central ridges in the vicinity of the true DOAs, along with varying ridges arising from the ghost DOAs. As shown in the center and right-hand panels, the DOA spectrum produced by the horizontal frequency axis suppresses ghost DOAs while leaving only stationary true DOAs. CFD significantly enforces the sparseness of the 2D map owing to l_1 -norm regularization, so the averaged DOA spectrum has a high resolution of the two sources.

The Rayleigh resolution limit [p. 48 of Van-Trees (2002)] for FD is calculated as $\Delta\theta_{FD} = \sin^{-1}(\Delta\lambda / Md) = 7.2^\circ$, implying that the sources should be at least 7.2° apart to be separated by FD. Figures 2(a) and 2(b) correspond to an optimistic case where the DOA difference is larger than the Rayleigh limit, whereas the opposite cases are shown in Figs. 2(c)–2(f). Both FD and CFD correctly resolve the two sources for a wide separation. CFD provides two sharp peaks. However, as the angular separation narrows below $\Delta\theta_{FD}$, the two main beams of the FD merge, eventually resulting in a biased estimation from the true DOAs [Fig. 2(c)]. In contrast, CFD can still resolve them at the correct DOAs with an improved resolution [Fig. 2(d)].

In the cases where sources are too close to each other, both FD and CFD exhibit a single false peak between the true DOAs [Figs. 2(e) and 2(f)]. The resolution limit analysis of CFD is similar to that of CS, analyzed by Xenaki et al. (2014) with the fidelity term in Eq. (7). The analysis states that any vector \mathbf{x} can be a possible solution for the problem with true solution \mathbf{x}_s if the following inequality holds:

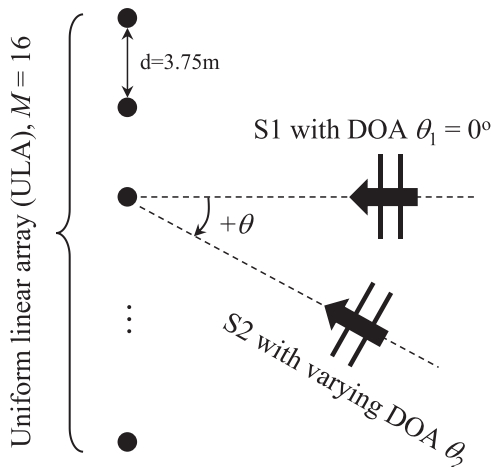


FIG. 1. Two-DOA simulation environment with $M=16$ ULA (sensor spacing $d=3.75$ m); one DOA θ_1 is fixed at 0° , while the other DOA θ_2 varies from 0° to 25° .

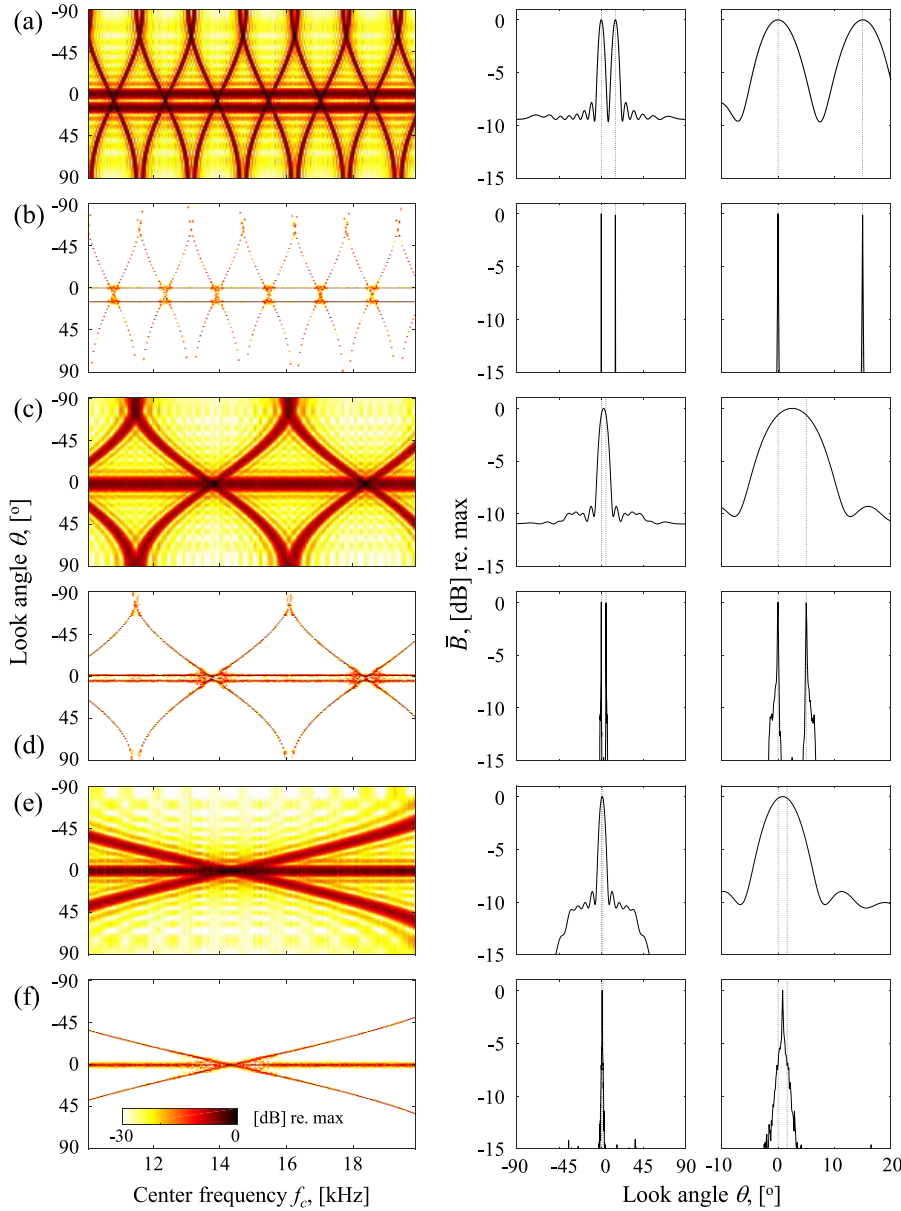


FIG. 2. (Color online) FD and CFD beamforming for multiple cases with different DOA differences between two sources. θ_1 is fixed at 0° , while the other varies: (a) $\theta_2 = 15^\circ$ with FD, (b) $\theta_2 = 15^\circ$ with CFD, (c) $\theta_2 = 5^\circ$ with FD, (d) $\theta_2 = 5^\circ$ with CFD, (e) $\theta_2 = 1.6^\circ$ with FD, and (f) $\theta_2 = 1.6^\circ$ with CFD. Left: Beamforming output B using Eq. (4) for FD and $B = |\hat{\mathbf{x}}_{CFD}|^2$ for CFD as a function of the look angle θ and center frequency f_c . Center: Incoherently averaged beampower \bar{B} using Eq. (6) for FD and Eq. (10) for CFD. Right: Zoomed-in view for the center. The results are averaged over $L = 20$ snapshots. Dotted lines represent true DOAs.

$$0 \leq \|\mathbf{A}(\mathbf{x} - \mathbf{x}_s)\|_2 \leq \varepsilon, \quad (12)$$

where ε is the upper bound for the noise norm such that $\|\mathbf{n}\|_2 \leq \varepsilon$. For two sources with equal strength, $x_s/4$, the strengths of the two associated ghost sources are also $x_s/4$. The term $\mathbf{A}\mathbf{x}_s$ is then represented as

$$\mathbf{A}\mathbf{x}_s = \frac{x_s}{4}(\mathbf{a}(\theta_1, \Delta f) + \mathbf{a}(\theta_2, \Delta f) + \mathbf{a}(\theta_{g1}, \Delta f) + \mathbf{a}(\theta_{g2}, \Delta f)). \quad (13)$$

A lack of resolution occurs whenever any possible pair among the four DOAs (θ_1 , θ_2 , θ_{g1} , and θ_{g2}) is resolved into one DOA. A practical scenario occurs when the two true DOAs are adjacent to each other while the ghost DOAs are away from them. That is, the four DOAs are resolved into three DOAs of θ_k with strength x , θ_{g1} , and θ_{g2} with

strengths $x_s/4$. Therefore, substituting $\mathbf{A}\mathbf{x} = x\mathbf{a}(\theta_k, \Delta f) + (x_s/4)(\mathbf{a}(\theta_{g1}, \Delta f) + \mathbf{a}(\theta_{g2}, \Delta f))$ and Eq. (13) into inequality [Eq. (12)] yields

$$\left\| x\mathbf{a}(\theta_k, \Delta f) - \frac{x_s}{4}(\mathbf{a}(\theta_1, \Delta f) + \mathbf{a}(\theta_2, \Delta f)) \right\|_2 \leq \varepsilon. \quad (14)$$

The optimal value of x minimizes the error norm,

$$q(x) = \|x\mathbf{a}(\theta_k, \Delta f) - (x_s/4)(\mathbf{a}(\theta_1, \Delta f) + \mathbf{a}(\theta_2, \Delta f))\|_2^2.$$

From the solution of $\partial q / \partial x = 0$,

$$x = \frac{x_s}{4} \mathbf{a}^H(\theta_k, \Delta f)(\mathbf{a}(\theta_1, \Delta f) + \mathbf{a}(\theta_2, \Delta f)), \quad (15)$$

the inequality [Eq. (14)] comes to

$$e_{CFD} = \frac{1}{4} \|\mathbf{a}(\theta_k, \Delta f)^H (\mathbf{a}(\theta_1, \Delta f) + \mathbf{a}(\theta_2, \Delta f)) \mathbf{a}(\theta_k, \Delta f) - \mathbf{a}(\theta_1, \Delta f) - \mathbf{a}(\theta_2, \Delta f)\|_2 \leq 2\rho, \quad (16)$$

where “ e ” denotes the error norm, and $\rho = 10^{-\text{SNR}/20}$ is the relative noise level. The maximum angular difference $|\theta_1 - \theta_2|$ satisfying inequality [Eq. (16)] is interpreted as the resolution limit of the CFD $\Delta\theta_{CFD}$. The counterpart for CS [Eq. (26) of Xenaki *et al.* (2014)] is

$$e_{CS} = \frac{1}{2} \|\mathbf{a}(\theta_k, f)^H (\mathbf{a}(\theta_1, f) + \mathbf{a}(\theta_2, f)) \mathbf{a}(\theta_k, f) - \mathbf{a}(\theta_1, f) - \mathbf{a}(\theta_2, f)\|_2 \leq 2\rho. \quad (17)$$

Except for the evaluation frequency of the steering vector, CFD [Eq. (16)] has a factor of 1/4 instead of 1/2 due to the two real sources and two ghost sources [see Eq. (13)]. Consequently, the resolution limit of CFD is twice that of CS for a given SNR.

Evaluation of e_{CFD} and its values up to 2ρ ($=6.32 \times 10^{-2}$ with $\text{SNR} = 30$ dB) are shown in Fig. 3. The contours indicate that CFD cannot distinguish two adjacent DOAs whose difference is less than $\Delta\theta_{CFD} = 2.2^\circ$. Figure 4 shows true DOAs versus estimated DOAs for the test range. FD begins to distinguish the two sources for DOA differences greater than $\Delta\theta_{FD} = 7.2^\circ$, whereas CFD exhibits a lower minimum separable angle of 2.2° . Thus, CFD achieves a high resolution beyond the Rayleigh limit of FD. In addition, CFD reports a positive outcome by providing smaller error amplitudes than FD. The DOA estimation with CFD is also overlaid on the map of e_{CFD} in Fig. 3(b). The origin of the separation can be traced to the region where e_{CFD} exceeds the value of 2ρ , which justifies the relation [Eq. (16)].

Thus, we can utilize the relation [Eq. (16)] to investigate the variation of $\Delta\theta_{CFD}$ with respect to SNR, as shown in Fig. 5. CFD loses its effectiveness in a noisy environment because the range of steering vectors satisfying inequality [Eq. (16)] expands with decreasing SNR. FD exhibits better separation performance for SNR below 4 dB, whereas CFD works well for SNRs that are not too low.

Next, the simulation assumes that the relative phase between the sources is 0° , which occurs in a multipath situation resulting in coherent arrivals. In contrast to Fig. 4(a),

the error dynamics of FD exhibit a damped oscillation [Fig. 6(a)]. This behavior is consistent with optics results [see Fig. 6 of Grimes and Thompson (1967)].

To explain such oscillation in a simple manner, we consider noiseless measurement from the two DOAs with unit strengths but with different phases,

$$\mathbf{y}(f_u) = e^{j\phi_{1u}} \mathbf{a}(\theta_1, f_u) + e^{j\phi_{2u}} \mathbf{a}(\theta_2, f_u), \\ \mathbf{y}(f_l) = e^{j\phi_{1l}} \mathbf{a}(\theta_1, f_l) + e^{j\phi_{2l}} \mathbf{a}(\theta_2, f_l),$$

where ϕ_{1u} , ϕ_{2u} , ϕ_{1l} , and ϕ_{2l} denote the phase angles for each DOA and frequency. Then the beamforming output of FD [Eq. (6)] can be written as

$$\bar{B}_{FD}(\theta) = E \left[|e^{j(\phi_{1u}-\phi_{1l})} \mathbf{a}_1^H \mathbf{a} + e^{j(\phi_{1u}-\phi_{1l})} \mathbf{a}_2^H \mathbf{a}|^2 \right]. \quad (18)$$

Here, the notation for the steering vector is simplified to $\mathbf{a}(\theta_i, \Delta f) = \mathbf{a}_i$. Note that ghost DOAs do not appear in Eq. (18) after the frequency averaging. It is easy to show that

$$\bar{B}_{FD}(\theta) = |b_1|^2 + |b_2|^2 = |\mathbf{a}_1^H \mathbf{a}|^2 + |\mathbf{a}_2^H \mathbf{a}|^2 \quad (19)$$

for incoherent sources (ϕ_{1u} , ϕ_{2u} , ϕ_{1l} , $\phi_{2l} \sim U[0, 2\pi]$), and

$$\begin{aligned} \bar{B}_{FD}(\theta) &= |\mathbf{a}_1^H \mathbf{a} + \mathbf{a}_2^H \mathbf{a}|^2 \\ &= |\mathbf{a}_1^H \mathbf{a}|^2 + |\mathbf{a}_2^H \mathbf{a}|^2 + (\mathbf{a}_1^H \mathbf{a})^* (\mathbf{a}_2^H \mathbf{a}) + (\mathbf{a}_2^H \mathbf{a})^* (\mathbf{a}_1^H \mathbf{a}) \\ &= \underbrace{|b_1|^2 + |b_2|^2}_{\text{auto(incoherent)-beampower}} + \underbrace{b_1^* b_2 + b_2^* b_1}_{\text{cross-beampower}} \end{aligned} \quad (20)$$

for fully coherent sources ($\phi_{1u} = \phi_{2u} = \phi_{1l} = \phi_{2l}$). The first two terms are designated as the auto(or incoherent)-beampower, since they represent a sum of the individual beamforming power. The latter two terms, designated as cross-beampower, represent the joint contributions of two DOAs, and they can cause interference effects as detailed below.

From Eq. (1), beamforming for each source yields

$$b_i = \frac{1}{M} \sum_{m=1}^M e^{-j\Delta kd(m-1)(\sin \theta - \sin \theta_i)} \quad (i = 1, 2),$$

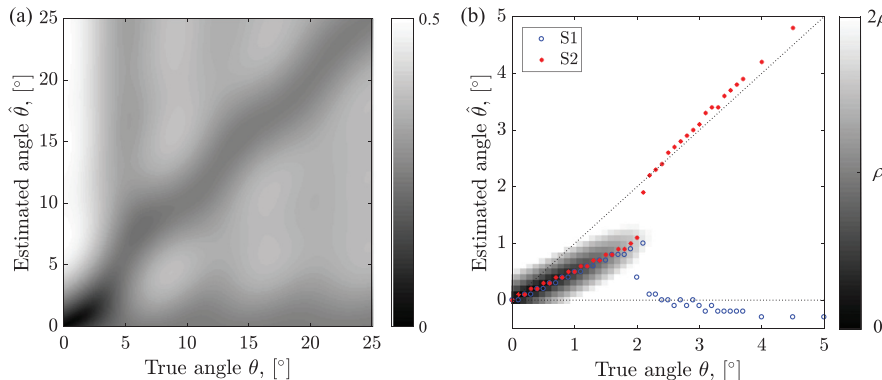


FIG. 3. (Color online) (a) Evaluation of e_{CFD} for $\text{SNR} = 30$ dB ($\rho = 6.32 \times 10^{-2}$). (b) Detail (0° – 5°) of (a) up to 2ρ with overlaying the estimated DOAs. The starting point of DOA separation corresponds with the point where the value of e_{CFD} surpasses 2ρ , justifying the relation [Eq. (16)].

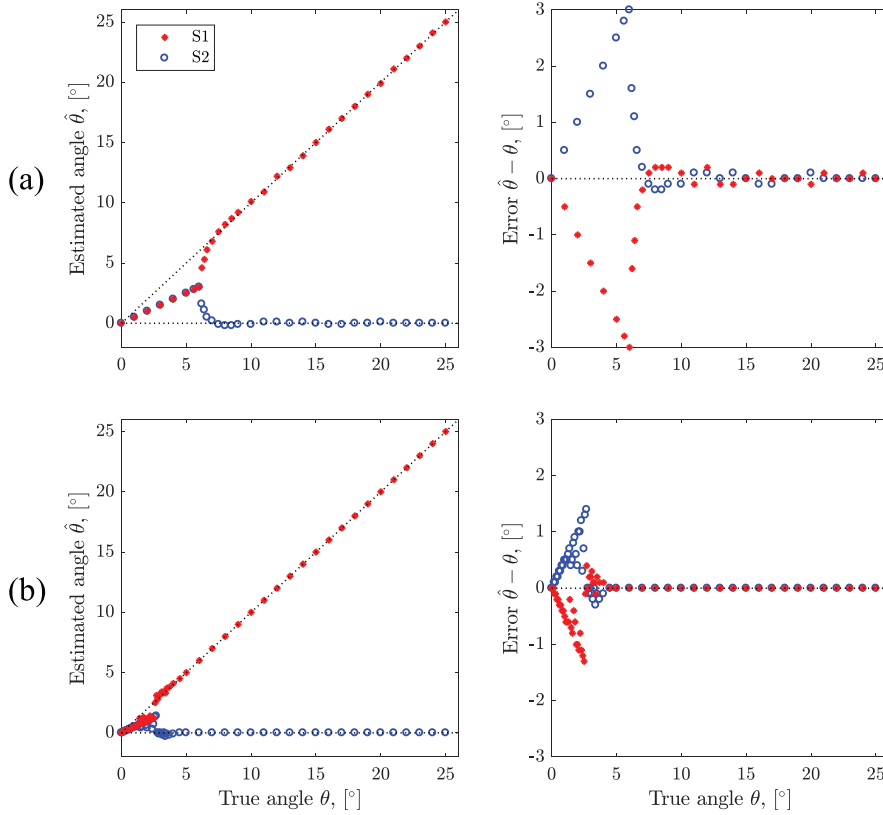


FIG. 4. (Color online) DOA estimation (left) and estimation error (right) with multiple snapshots ($L=20$) (a) FD and (b) CFD (incoherent sources, SNR = 30 dB).

where $\Delta k (=2\pi\Delta f/c)$ is the wavenumber corresponding to Δf . The alternative form of b_i using the trigonometric identity $\sum_{m=0}^{M-1} e^{-jmx} = \sin(Mx/2)/\sin(x/2)e^{-j(M-1)x/2}$ is

$$b_i = \frac{1}{M} \frac{\sin((\sin\theta - \sin\theta_i)M\Delta kd/2)}{\sin((\sin\theta - \sin\theta_i)\Delta kd/2)} \times e^{-j(\sin\theta - \sin\theta_i)(M-1)\Delta kd/2}.$$

Even for half-wavelength sensor spacing ($d=\Delta\lambda/2$), the argument $(\sin\theta - \sin\theta_i)\Delta kd/2$ can be assumed to be small for approximately $\theta_i - 30^\circ < \theta < \theta_i + 30^\circ$. Thus, b_i is approximated by

$$b_i \approx \text{sinc}((\sin\theta - \sin\theta_i)M\Delta kd/2) e^{-j(\sin\theta - \sin\theta_i)(M-1)\Delta kd/2}. \quad (21)$$

Accordingly, the cross-beampower is as follows:

$$b_1^* b_2 + b_2^* b_1 = 2 \text{sinc}((\sin\theta - \sin\theta_1)M\Delta kd/2) \times \text{sinc}((\sin\theta - \sin\theta_2)M\Delta kd/2) \times \cos((\sin\theta_2 - \sin\theta_1)(M-1)\Delta kd/2). \quad (22)$$

As a result of the multiplication of sinc functions, the cross-beampower generates two strong local maxima at angular locations that are not the true DOAs. When the cross-beampower is added to the auto-beampower, the resultant total beampower has no choice but to offset the DOA estimation. Figure 7 shows an example for $\theta_1 = 0^\circ$, $\theta_2 = 8^\circ$, and Fig. 8 shows all test DOAs. The cosine term in Eq. (22) shows that the effect of cross-beampower varies periodically with the look angle (θ) and DOA separation ($|\theta_1 - \theta_2|$) [see Fig. 8(a)]. The oscillation period along the DOA separation is calculated as $\sin^{-1}(\Delta\lambda/d(M-1)) = 7.6^\circ$. When the DOA separation is wide, the cosine term vanishes, and the cross-beampower has no effect. This explains why the DOA

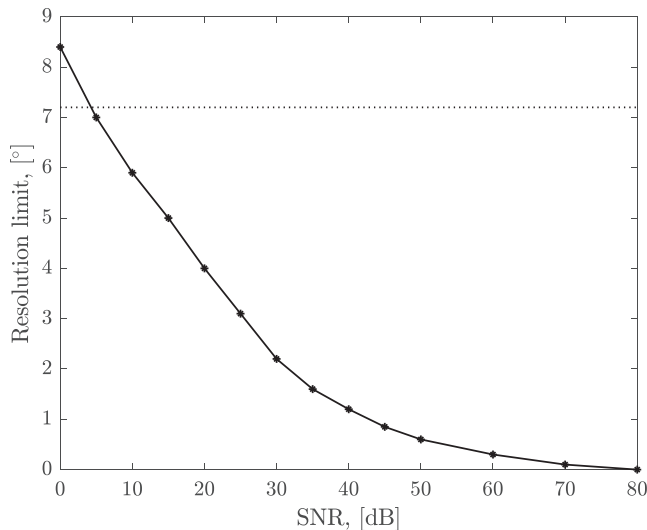


FIG. 5. CFM resolution limit ($\Delta\theta_{CFM}$) for two DOAs versus SNR. The Rayleigh resolution limit $\Delta\theta_{FD} = 7.2^\circ$ is depicted with the dotted line. Note that $\Delta\theta_{FD}$ is independent of SNR.

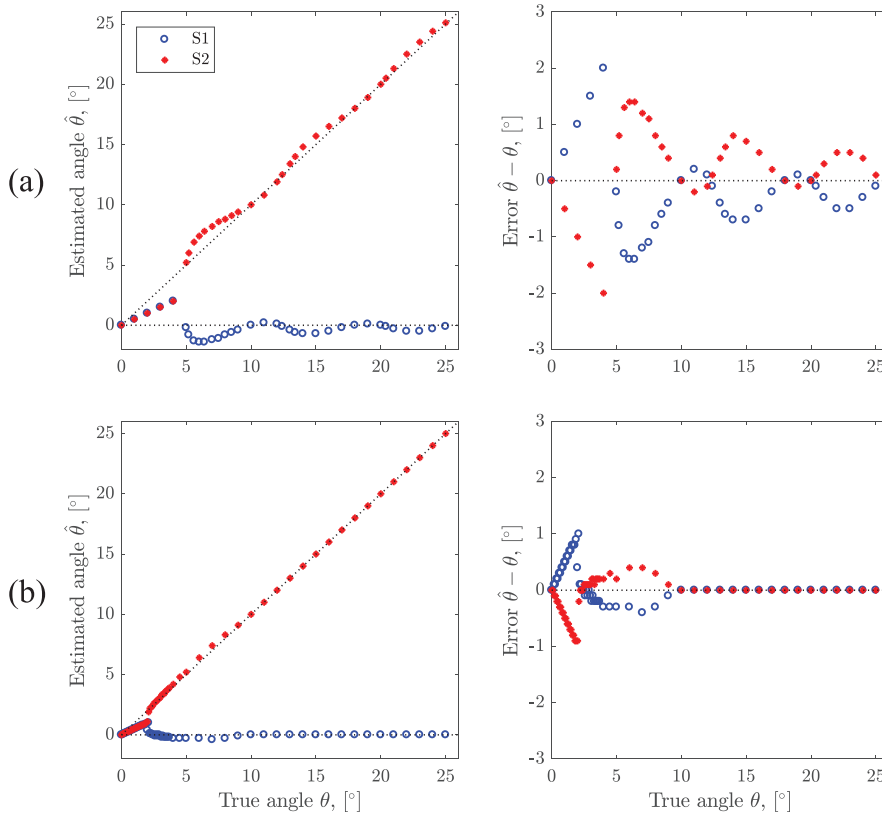


FIG. 6. (Color online) DOA estimation (left) and estimation error (right) with multiple snapshots ($L=20$) (a) FD and (b) CFD (coherent sources, SNR = 30 dB).

estimation error for coherent arrivals [Fig. 6(a)] exhibits a damped oscillation.

CFD is not affected by source correlation or cross-power contamination. Therefore, the proposed method estimates the two DOAs accurately without any error oscillation, as long as the DOA difference is a bit above $\Delta\theta_{CFD}$ [Fig. 6(b)]. Figure 9 shows that even with a single snapshot ($L=1$), CFD remains stable and performs well in challenging scenarios with coherent arrivals and a limited number of snapshots.

B. Focused acoustic field (FAF06) experiment

To experimentally demonstrate the performance of CFD, both FD and CFD are applied to ocean acoustic

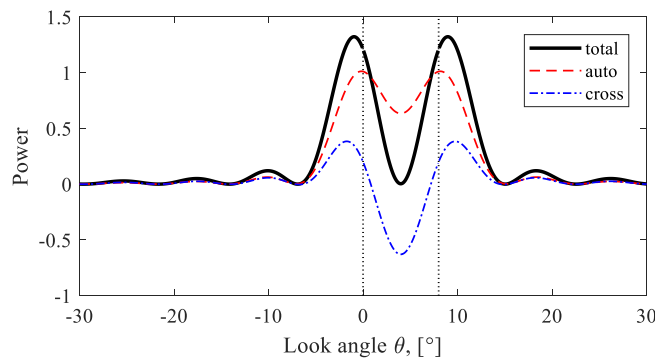


FIG. 7. (Color online) Coherent B_{FD} decomposition into auto- and cross-beampower for two DOAs $\theta_1=0^\circ$ and $\theta_2=8^\circ$. Auto-beampower (red dashed line) and cross-beampower (blue dashed-dotted line) are based on Eqs. (19) and (22), respectively. Total (black heavy line) beampower is their summation. Dotted lines represent true DOAs.

measurements (Figs. 10 and 11). The data used were from the FAF06 experiment (Song *et al.*, 2009; Song *et al.*, 2010), which utilized a vertical ULA with the same geometry as in Sec. III A. The array spans an aperture of 56.25 m and is centered at a depth of 52.8 m in 92 m deep water. Except for a few of the shallowest receivers in the thermocline layer, most receivers are in the region where the sound speed is constant at $c=1510$ m/s. The sampling frequency f_s is 50 kHz.

The primary purpose of FAF06 is to record the broadcast signal emitted by an acoustic projector located far from the array. However, unintended bursting noise, which is not a part of the FAF06 signal broadcasting, is frequently captured in the recorded data. The source of this noise could be small biological creatures (Yuan *et al.*, 2018) or the interactive friction between the array cable and mooring buoy (Abadi *et al.*, 2012). Each bursting consists of a direct arrival characterized by a strong impulse, followed by a sea-surface reflected arrival with a non-impulsive (dispersive) character. In this study, two cases are demonstrated by selecting or synthesizing bursting events.

Figure 10(a) shows the signal chosen for the first demonstration. A high-pass filter with a cutoff frequency of 9 kHz is used to highlight the signal structure. The preceding signal exhibits a spherical-like wavefront, and its apparent DOA ranges from $+1.1^\circ$ to $+3.3^\circ$. In contrast, the subsequent reflection, with a plane wave nature, is received with an apparent DOA of -17° . As the difference in the apparent DOAs is approximately 20° , the first demonstration is considered as a wide-separation case. It is worth noting that the

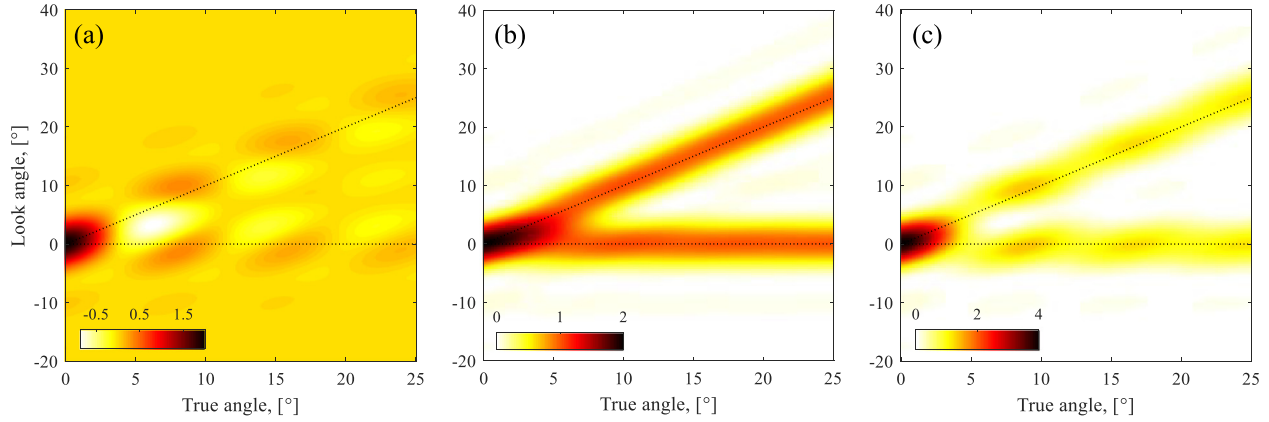


FIG. 8. (Color online) Coherent B_{FD} decomposition into auto- and cross-beampower for the entire test DOAs. (a) Cross-beampower [Eq. (22)]; (b) auto(incoherent)-beampower [Eq. (19)]; (c) total beampower (= cross + auto). Dotted lines represent true DOAs.

waterfall plot of the measured waveform provides clear DOAs without the need for beamforming. The data in Fig. 10(a) [and Fig. 11(a)] are solely for verification, as our objective is to compare the performance of FD and CFD.

The spectral data obtained from a 2048 ($= N_{fft}$)-point fast Fourier transform were analyzed using single-snapshot FD and CFD for the angular search domain of $\theta = [-90^\circ: 0.5^\circ: 90^\circ]$, $N = 361$. The frequency setup, $\Delta f = 0.2$ kHz, $f_L = 10$ kHz, and $f_U = 20$ kHz, is identical to those used in Sec. III A. However, the overlapping rule in Eq. (11) is slightly modified to accommodate discrete spectral data spaced by f_s/N_{fft} as follows:

$$\begin{aligned} f_l &= (f_s/N_{fft})(n_{f_L} + (i-1)(n_{\Delta f} - q')) \\ f_u &= (f_s/N_{fft})(n_{f_L} + (i-1)(n_{\Delta f} - q') + n_{\Delta f}) \\ (i &= 1, 2, \dots, F'), \end{aligned} \quad (23)$$

where n_x denotes the nearest integer multiple of f_s/N_{fft} such that $n_x = \text{round}(x/(f_s/N_{fft}))$, $q' (\leq n_{\Delta f})$ is the number of overlapping frequency bins, and $F' = 1 + (n_{f_U} - n_{f_L} - n_{\Delta f})/(n_{\Delta f} - q')$ is the number of difference-frequency pairs. q' is set as 6 (75% overlapping), yielding $F' = 201$. The regularization parameter μ for CFD is set to a constant value of 0.25.

In the 2D map of FD [left side of Fig. 10(b)], two stationary DOA components are visible. The estimated DOAs match the apparent DOAs, as shown in the incoherent average of the FD output on the right side of Fig. 10(b). CFD provides a clear 2D map with two streaks, and its DOA spectrum exhibits two sharp peaks with suppressed side-lobes [see Fig. 10(c)]. [For enhanced visibility of the sparse result, Fig. 10(d) displays an image obtained from the 2D-convolution of B_{CFD} , left of Fig. 10(c), with a 3×3 ones matrix.] The interference pattern for both FD and CFD is less apparent than the simulation but in agreement with Abadi *et al.* (2012) [see Fig. 9(b)].

The second demonstration deals with a scenario with narrow separation of DOAs to show the superiority of CFD. The time record for this case is synthesized by clipping two sea-surface reflections from the original record and then joining them. As shown in Fig. 11(a), there are two arrival groups with apparent DOAs of -12° and -17° . Except for $\mu = 0.30$, all processing parameters remain the same as in the wide-separation case.

The 2D map of FD in Fig. 11(b) is featureless compared to that of Fig. 10(b). A small DOA difference causes the associated beams to randomly interfere with each other in either a constructive or destructive manner. Thus, the ridge

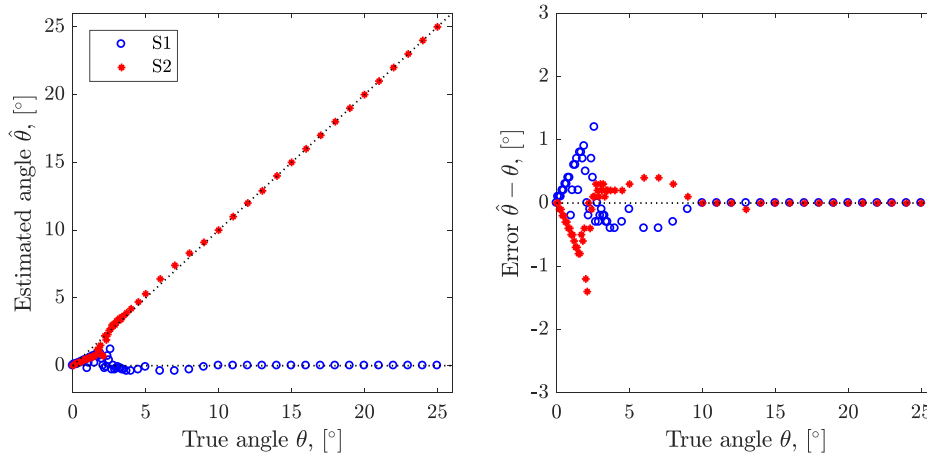


FIG. 9. (Color online) DOA estimation (left) and estimation error (right) with single-snapshot ($L = 1$) CFD (coherent sources, SNR = 30 dB).

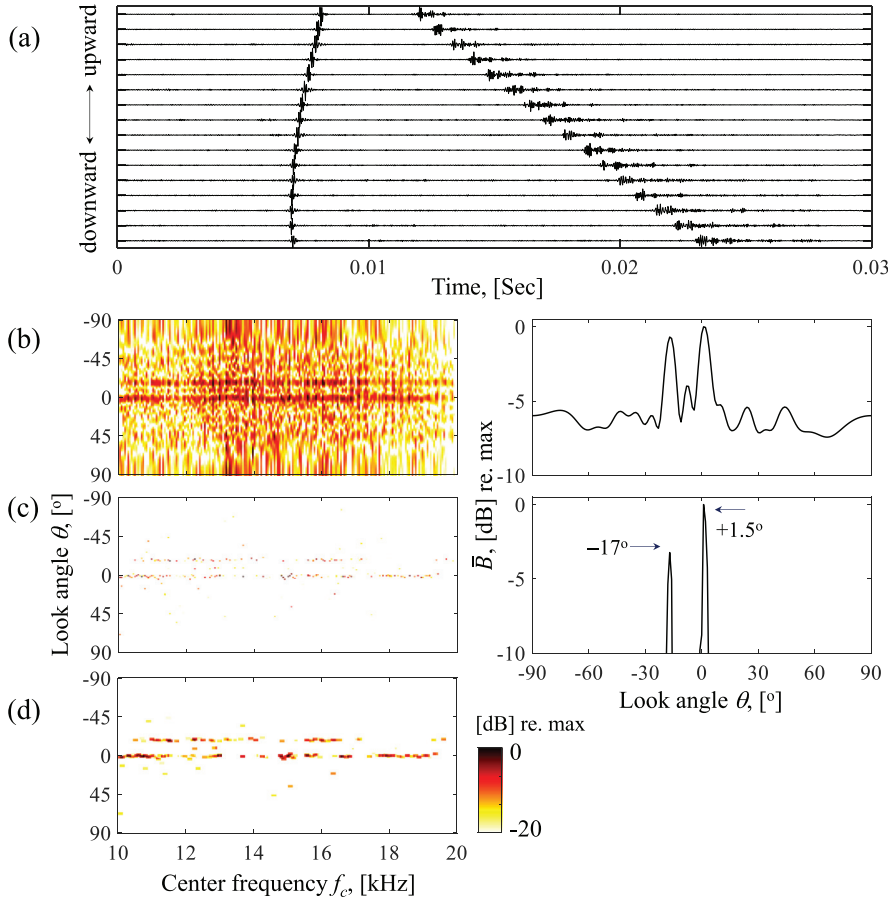


FIG. 10. (Color online) Experimental demonstration for widely separated DOAs: (a) received time record along the vertical array (the shallowest receiver in the top pressure time trace is at a depth of 24.675 m, and the deepest receiver is at a depth of 80.925 m); (b) B_{FD} (left) and \bar{B}_{FD} (right); (c) B_{CFD} (left) and \bar{B}_{CFD} (right); (d) image obtained from 2D-convolution of B_{CFD} [left of (c)] with a 3×3 ones matrix.

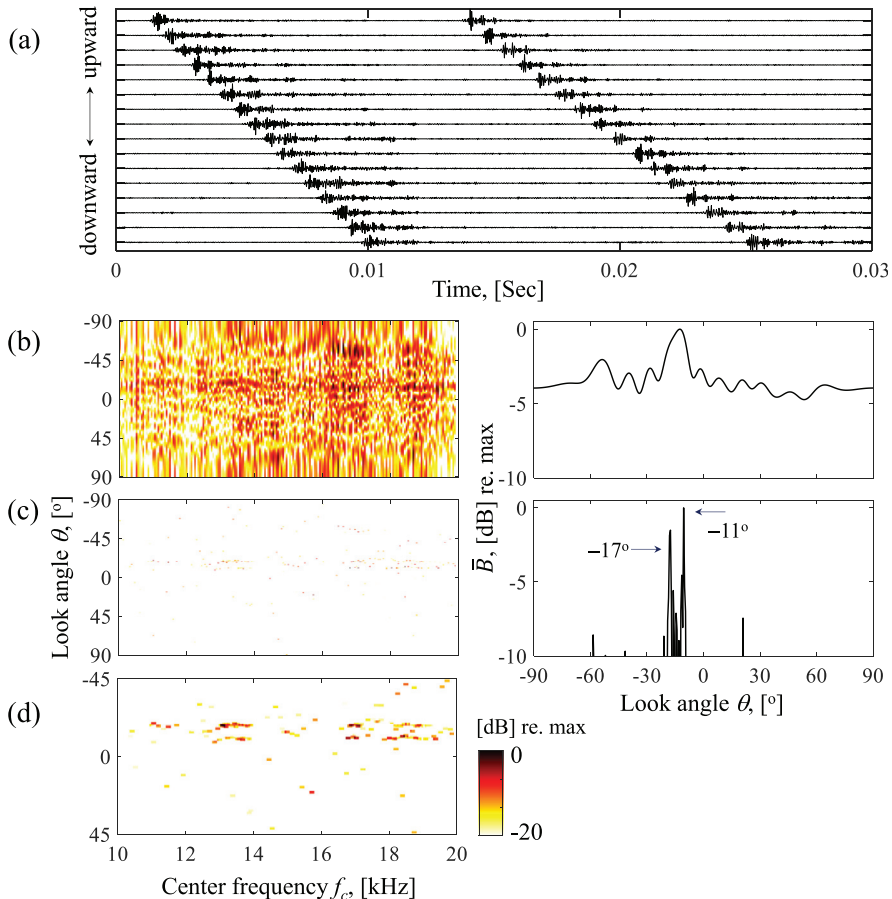


FIG. 11. (Color online) Experimental demonstration for narrowly separated DOAs: (a) time record synthesized by clipping two non-impulsive signals from the original record and then joining them together (the shallowest receiver in the top pressure time trace is at a depth of 24.675 m, and the deepest receiver is at a depth of 80.925 m); (b) B_{FD} (left) and \bar{B}_{FD} (right); (c) B_{CFD} (left) and \bar{B}_{CFD} (right); (d) image obtained from 2D-convolution of B_{CFD} [left of (c)] with a 3×3 ones matrix (zoomed between $\theta = -45^\circ$ and 45°).

around the expected DOAs fluctuates randomly along the frequency, making it difficult to identify the spurious map. The DOA spectrum of FD generates not only a single blunt peak around the look angle of -13° but also higher side-lobes. In contrast, CFD provides an improved interpretation [see Figs. 11(c) and 11(d)]. In the CFD map, the areas with high values generally coincide with the regions where the output of FD is also high. More importantly, the resolution-improving capability still yields two fine streaks on the map. The subsequent DOA spectrum distinguishes the two arrivals of interest, supporting the validity of the proposed method.

IV. CONCLUSION

FD enables DOA estimation of high-frequency sources without spatial aliasing. However, it often fails to distinguish closely spaced DOAs due to the lowered processing frequency, the difference-frequency Δf . This study suggests a resolution-improving method for FD. We propose CFD beamforming, which imposes a sparsity-promoting constraint on FD in the form of the LASSO problem. The simulation analysis confirms that CFD outperforms FD in terms of separation for not too low SNR. The performance of the method is also demonstrated through experimental data. Therefore, CFD serves as a complementary tool in challenging situations where FD is inappropriate.

ACKNOWLEDGMENTS

This work was supported in part by the National Research Foundation of Korea (NRF) under Grant No. 2021R1A2C1005962, in part by the Korea Institute of Marine Science and Technology Promotion (KIMST) Grant No. 20210500, and in part by the Office of Naval Research under Grant No. N00014-21-1-2267. The authors would also like to thank Dr. Hee-Chun Song for helping with data access for the FAF06 experiment.

- Abadi, S. H., Song, H. C., and Dowling, D. R. (2012). "Broadband sparse-array blind deconvolution using frequency-difference beamforming," *J. Acoust. Soc. Am.* **132**, 3018–3029.
- Candes, E., and Romberg, J. (2005). " ℓ_1 -MAGIC: Recovery of sparse signals via convex programming," <https://candes.su.domains/software/l1magic/> (Last viewed February 7, 2023).
- Capon, J. (1969). "High-resolution frequency-wavenumber spectrum analysis," *Proc. IEEE* **57**, 1408–1418.
- Douglass, A. S., and Dowling, D. R. (2019). "Frequency-difference beamforming in the presence of strong random scattering," *J. Acoust. Soc. Am.* **146**, 122–134.
- Douglass, A. S., Song, H. C., and Dowling, D. R. (2017). "Performance comparisons of frequency-difference and conventional beamforming," *J. Acoust. Soc. Am.* **142**, 1663–1673.
- Geroski, D. J., and Dowling, D. R. (2019). "Long-range frequency-difference source localization in the Philippine Sea," *J. Acoust. Soc. Am.* **146**, 4727–4739.
- Geroski, D. J., Dzieciuch, M. A., and Dowling, D. R. (2021). "Measurements of the correlation of the frequency-difference autoprodut with acoustic and predicted-autoprodut fields in the deep ocean," *J. Acoust. Soc. Am.* **149**, 853–865.
- Geroski, D. J., and Worthmann, B. M. (2021). "Frequency-difference autoprodut cross-term analysis and cancellation for improved ambiguity surface robustness," *J. Acoust. Soc. Am.* **149**, 868–884.
- Gerstoft, P., Mecklenbräuker, C. F., Seong, W., and Bianco, M. (2018). "Introduction to compressive sensing in acoustics," *J. Acoust. Soc. Am.* **143**, 3731–3736.
- Gerstoft, P., Xenaki, A., and Mecklenbräuker, C. F. (2015). "Multiple and single snapshot compressive beamforming," *J. Acoust. Soc. Am.* **138**, 2003–2014.
- Grant, M., and Boyd, S. (2014). "CVX: Matlab software for disciplined convex programming (version 2.1)," <http://cvxr.com/cvx> (Last viewed February 7, 2023).
- Grimes, D. N., and Thompson, B. J. (1967). "Two-point resolution with partially coherent light," *J. Opt. Soc. Am.* **57**(11), 1330–1334.
- Kim, D., Byun, G., and Kim, J. (2023). "Direction-of-arrival estimation based on frequency difference–wavenumber analysis for sparse vertical array configuration," *Sensors* **23**, 337.
- Kim, Y., and Nelson, P. A. (2004). "Optimal regularisation for acoustic source reconstruction by inverse methods," *J. Sound Vib.* **275**, 463–487.
- Krim, H., and Viberg, M. (1996). "Two decades of array signal processing research: The parametric approach," *IEEE Signal Process. Mag.* **13**, 67–94.
- Malioutov, D., Member, S., Çetin, M., and Willsky, A. S. (2005). "A sparse signal reconstruction perspective for source localization with sensor arrays," *IEEE Trans. Signal Process.* **53**, 3010–3022.
- Park, Y., Gerstoft, P., and Lee, J.-H. (2022). "Difference-frequency MUSIC for DOAs," *IEEE Signal Process. Lett.* **29**, 2612–2616.
- Schmidt, R. (1986). "Multiple emitter location and signal parameter estimation," *IEEE Trans. Antennas Propagat.* **34**, 276–280.
- Song, H. C., Hodgkiss, W. S., Kuperman, W. A., Akal, T., and Stevenson, M. (2009). "High-frequency acoustic communications achieving high bandwidth efficiency," *J. Acoust. Soc. Am.* **126**, 561–563.
- Song, H. C., Kim, J. S., Hodgkiss, W. S., Kuperman, W. A., and Stevenson, M. (2010). "High-rate multiuser communications in shallow water," *J. Acoust. Soc. Am.* **128**, 2920–2925.
- Tibshirani, R. (1996). "Regression shrinkage and selection via the lasso," *J. R. Stat. Soc. Series B Stat. Methodol.* **58**, 267–288.
- Van-Trees, H. L. (2002). *Optimum Array Processing: Part IV of Detection, Estimation, and Modulation Theory* (Wiley, New York), pp. 17–89.
- Wang, X., Sun, H., Zhang, L., Dong, C., and Guo, L. (2022). "Unambiguous broadband direction of arrival estimation based on improved extended frequency-difference method," *J. Acoust. Soc. Am.* **152**, 3281–3293.
- Worthmann, B. M., and Dowling, D. R. (2017). "The frequency-difference and frequency-sum acoustic-field autoproduts," *J. Acoust. Soc. Am.* **141**, 4579–4590.
- Worthmann, B. M., Song, H. C., and Dowling, D. R. (2015). "High frequency source localization in a shallow ocean sound channel using frequency difference matched field processing," *J. Acoust. Soc. Am.* **138**, 3549–3562.
- Wright, S. J., Nowak, R. D., and Figueiredo, M. A. T. (2009). "Sparse reconstruction by separable approximation," *IEEE Trans. Signal Process.* **57**, 2479–2493.
- Xenaki, A., Gerstoft, P., and Mosegaard, K. (2014). "Compressive beamforming," *J. Acoust. Soc. Am.* **136**, 260–271.
- Xie, L., Sun, C., and Tian, J. (2020). "Deconvolved frequency-difference beamforming for a linear array," *J. Acoust. Soc. Am.* **148**, EL440–EL446.
- Yang, L., Wang, Y., and Yang, Y. (2021). "Aliasing-free broadband direction of arrival estimation using a frequency-difference technique," *J. Acoust. Soc. Am.* **150**, 4256–4267.
- Yang, T. C. (2018). "Deconvolved conventional beamforming for a horizontal line array," *IEEE J. Ocean. Eng.* **43**, 160–172.
- Yuan, Z., Richards, E. L., Song, H. C., Hodgkiss, W. S., and Yan, S. (2018). "Calibration of vertical array tilt using snapping shrimp sound," *J. Acoust. Soc. Am.* **144**, 1203–1210.